minerals

Article

Mineralogy and Geochemistry (HFSE and REE) of the Present-Day Acid-Sulfate Types Alteration from the Active Hydrothermal System of Furnas Volcano, São Miguel Island, The Azores Archipelago

Iuliu Bobos [1,*] and Celso Gomes [2]

[1] ICTerra, DGAOT, Faculdade de Ciências, Universidade do Porto, Rua do Campo Alegre 687, 4168-007 Porto, Portugal

[2] Geobiotec, Departamento de Geociências, Universidade de Aveiro, 3810-193 Aveiro, Portugal; cgomes@ua.pt

* Correspondence: ibobos@fc.up.pt

Abstract: Acid-sulfate alteration is comprised by clays, sulfate, sinter and native sulphur minerals crystallized as neoformation products from dissolution of primary minerals during water-rock interaction. Smectite, kaolinite, halloysite-7 Å and opal-A occur in assemblages with alunite. Smectite represents a mechanical mixture between two (propylitic and acid-sulfate) alteration types. High amounts of high-field strength elements (HFSE) and rare earth elements (REE) were measured in acid-sulfate rocks. The Nb vs. Ta and Zr vs. Hf show a positive trend and a widely scattered relationships, suggesting a large fractionation during acid-sulfate alteration. Higher $\sum$REE amounts (up to 934.5 ppm) were found in clay-sulfate assemblages and lower $\sum$REE amounts in sinter (opal-A $\pm$ sulfate, 169.05 ppm) than to fresh rocks (up to 751.2 ppm). The acid-sulfate rocks reveal a distinctive gull-wing chondrite-normalized pattern with a negative Eu anomaly and light- and heavy-REE "wings" similar to the gull-wing pattern of fresh rocks. The Eu/Eu* shows a large fractionation of acid sulfate rocks from 0.16 to 0.78 with respect to fresh trachyte products (0.10 to 0.38). Variation of $(La/Sm)_N$ and $(La/Yb)_N$ ratio show a large fractionation of light-REE and heavy-REE. The Y vs. Dy and Y vs. Ho show a very good positive correlation coefficient and a large Y fractionation in acid-sulfate rocks with respect to fresh rocks.

Keywords: acid-sulfate alteration; sinter; alunite and clays; high-field strength and rare earth elements; São Miguel island; Azores archipelago

1. Introduction

Acid sulfate–type alteration is associated with geothermal systems related to volcano-plutonic activity along to convergent and divergent plate boundaries, where steam condensate forms and mixes with meteoric water encouraging intensive water-rock interaction and silicate hydrolysis, typically at high water-to-rock ratios [1–6]. Fluid discharged at the surface corresponds to near-neutral chloride-rich hot spring waters or to acid-sulfate boiling pools related to steam that separates from deeper chloride-rich boiling fluids in vapour dominated systems resulting in fumarolic activity containing CO_2 and H_2S [6–8].

Low pressure favors high SO_2/H_2S and $HCl/NaCl$ in the emitted magmatic vapors, increasing the acidity of near-surface condensate [9,10]. The acid formation is further favored where crater lakes occur at the surface, as the supply of capping groundwater to minimizes the possibility that the gas-steam mixture can escape directly to the atmosphere [11]. Thermodynamically, the acid-sulfate alteration stage is connected with the low-enthalpy (T < 200 °C) water resources, representing a much larger potential and a wider regional distribution than high-enthalpy resources [12].

Such environments are highly analogous and inseparable from the high-sulfidation environments responsible for some types of epithermal ore formation [5,13,14]. Steadily,

acid-sulfate alteration occurs also in and around many epithermal ore deposits occurring in the same tectonic setting context, where enargite, pyrite, covellite among others may precipitate [15]. However, the dominant material is represented by various forms of silica [11,13,16,17] in the most acid-altered areas, which may convert from amorphous silica (opal-A) to a more pseudo (crypto)- or crystalline forms of silica, including opal-CT, opal-C, chalcedony and quartz [18,19]. Other minerals may include alunite, kaolinite and anatase. Such rocks contain >90% SiO_2 primarily own to a near-total dissolution of the rocks by the strong (mostly sulfuric) acid [14,20].

Fascinating active acid-sulfate environments associated to endogenous degassing (i.e., H_2O, CO_2, CH_4, H_2S, SO_2, HCl, HF, etc.) and hot water fluid circulation (hydrothermal/geothermal systems) were described around the world [1,21–27]. One of these places is connected with the post-volcanic activity related to the evolution of Furnas volcano, São Miguel Island. Fumaroles, hot springs and steaming grounds manifested at the surface are associated to an active hydrothermal system below the Furnas volcano, where the distribution of fumaroles and hot-springs appears to be controlled by a regional fault systems [28,29]. Present-day fumaroles and hot springs activity in the Furnas volcano produced an acid-sulfate alterations, where the volcanic rocks are argillic altered to a porous siliceous residue due to an intensive acid leaching. The hydrothermal waters discharged derive from local precipitation after 10% steam fractionation in the fumarole conduits [29]. Furthermore, hydrothermal-meteoric waters without any magmatic fluid contribution were identified in the Furnas volcano, where the chemical flux shows that the degassing carbon dioxide leached silica and sodium dominated the released material [30].

Hence, the main goal of this work is to carry out a detailed mineralogical study and to characterize the HFSE and REE geochemistry of the acid-sulfate stage from several areas related to Furnas volcano.

2. Geology

The Azores archipelago is located close to the Mid-Atlantic Ridge, where the three lithospheric plates (American, Eurasian and African) are jointed as a triple junction [31–33]. The nine islands of the Azores archipelago (Figure 1a) are constituted by trachyte pyroclastic rocks deposited during several phases of Plinian and sub-Plinian eruption type [34]. The volcanic products range in composition from basanite to trachyte, where the products erupted within caldera complex are trachytic in composition consisting of trachyte and latite [34,35].
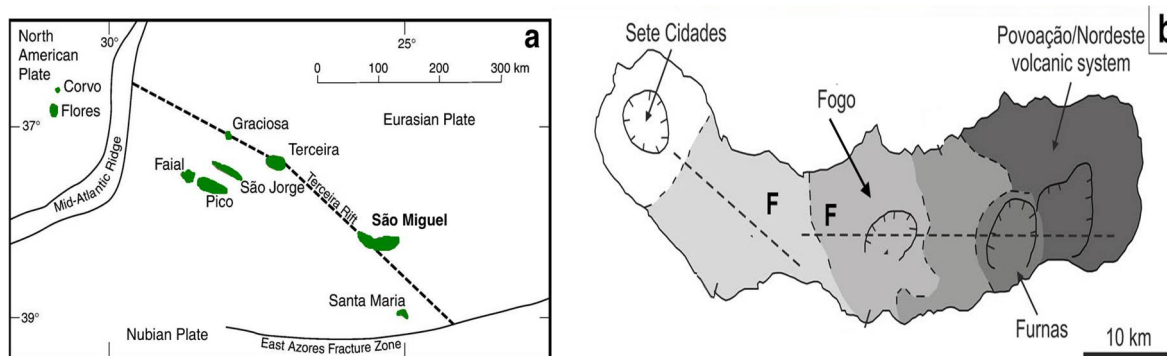

Figure 1. *Cont.*
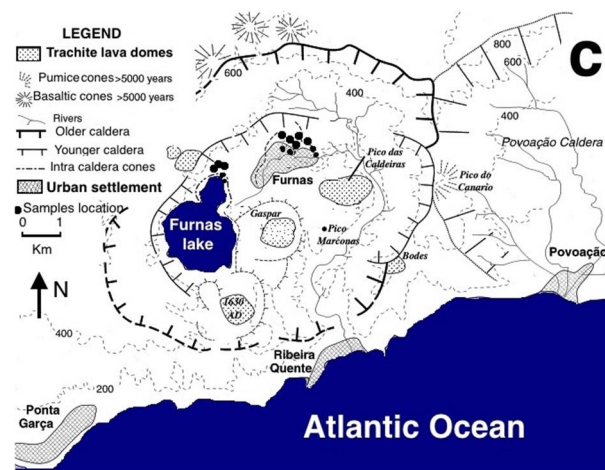
Figure 1. (**a**) Major tectonic features of Azores triple junction [36]. (**b**) The volcanological map of São Miguel [34,37], F-faults; (**c**) The simplified geological map of the craterial area of Furnas volcano [38,39].

The São Miguel Island, one of the nine islands, is constituted by three major trachytic central volcanoes of Furnas, Fogo and Sete Cidades (Figure 1b) linked by rift zones, where the volcanic activity along the rift is represented by basaltic effusive eruptions accompanied by a strombolian cone building [34]. Since 1970, detailed studies led to considerable advances regarding to a thorough knowledge of the explosive volcanism [35] and of the tephra deposits stratigraphy from all volcanic eruptions in the São Miguel island [40].

Furnas, one of the most active and hazardous volcanoes, has exhibited effusive (dome forming) to highly explosive (caldera-forming) eruptions of felsic magmas [38,39,41] during its subaerial existence. Volcanism within the caldera complex has been exclusively trachyte in composition, with mafic products being limited to vents on the volcano's flanks. The geology of the Furnas stratovolcano (Figure 1c) is constituted by an accumulation of trachyte and trachybasaltic lava flows with an episodic character, changing during 15,000 years from Plinian to sub-Plinian type [34].

The volcanic products range from basanite through alkali olivine basalt, potassic trachybasalt, basalt trachyandesite (shoshonite), trachyandesite (latite) to trachyte [39]. The pyroclastic rocks are trachyte in composition, consisting of latite and trachyte rocks within the caldera complex of Furnas volcano, where vents erupting basic lava are restricted to the flanks of the volcano.

The stratigraphy of Furnas volcanic complex was divided in three groups [39], such as: Lower Furnas group (Amoras Formation and Povoação ignimbrite Formation, −30,000 BP), Middle Furnas group (Mouco Formation, Ponta Graça Ignimbrite Formation and Cancelinha Formation, 12,000 BP) and Upper Furnas group (1630 AD).

The Upper Furnas Group (UFG) is build-up of at least ten intra-caldera, sub-Plinian eruptions of trachyte pumice, named Furnas A to J, where the latter, younger in age [40], is also known as Furnas AD 1630 [38,39,41]. Three of these eruptions correspond to lava domes in their final stages (Furnas E, I, and J) [38]. The dominant lithologies of the UFG consist of inter-bedded pumice lapilli and ash beds, inferred to be the result of a complex transition between magmatic and phreatomagmatic activity during eruption, whereas Furnas H is consisted exclusively by magmatic activity [38,39].

The main WNW–ESE fracture systems identified crosses the volcanic structure, including a conjugate faults system with N–S and NE–SW trends well-represented to the south coast [39].

Post-volcanic activity is characterized by hot springs, boiling pools, gassy cold springs as well as fumarolic fields referring to the areas of several hydrothermal systems related to the Quaternary volcanoes of Furnas, Fogo and Sete Cidades [42]. The post-volcanic activity in the Furnas volcanic complex was firstly described by Zbyszewski [43], where hot springs related probably to caldera-bounding fault [35] can be observed around to the

Lagoa of Furnas, the village of Furnas and along the upper Ribeira Quente brook at Ribeira dos Tambores close to the western bank of the brook. Hydrothermal features are naturally discharging water, e.g., including water-rich like boiling pools, thermal springs, as well as steam vents in total dissolved solids. The physic and chemical characteristics of thermal waters from fumaroles, boiling pools or hot springs are exposed in several works [29,30,44]. The gaseous composition of fumarolic grounds consist mainly of CO_2 with minor amounts of H_2S and N_2, where chemical flux of carbon dioxide estimated is about 9358 tons/yr [30].

3. Materials and Methods

3.1. Sampling and Field Observation

Altered volcanic rocks were collected from outcrops around to low-temperature fumaroles and steaming grounds from Caldeiras-Furnas village and Lagoa das Furnas, both located in the intracraterial area of Furnas's volcano. Two fresh trachyte rocks were collected for mineralogical and chemical analyses, one of this is a glassy pumice and is defined hereafter as "trachyte pumice".

Caldeiras-Furnas village area, ca +229 m altitude. The largest and representative area (several hundred square meters) of fumarole activity in the São Miguel islands occurs in the Furnas village located within the craterial area of Furnas volcano. Boiling fumaroles with steam explosions and steam heated pools (Figure 2a) of a mixed hydrothermal and surface waters are discharged at the surface. Interaction between fumarolic acid plume and the ground surface (Figure 2b) and outcropping rocks (e.g., pumice and trachyte) at a pH about 2–3 is well observed by the widespread acid-sulfate alteration in the proximal areas. Colour changes from yellowish, reddish or bloody to white of the acid-sulfate rocks was observed as an impressive peculiarity (Figure 2c). Also, finest veins exhibiting green to blue colour within white sulfate or argillic rocks were observed. Sinter interbeddings of 2–3 cm thickness precipitated directly from solutions occurs near to stream lines of Ribeira Quente brook.

Lagoa das Furnas (Furnas lake) area, ca +323 m altitude. Fumarole activity and steaming grounds are well spread around the Furnas's lakes (Figure 2d). The area is well exploited within magnify scenery, where local people take advantage of fumarole activity for cooking (the so-called "cozido") of the traditional gastronomy. Steaming grounds are characterized by mud-rich amorphous phase and hallloysite-7Å. Several locations were recognized where mixture of steaming grounds and sulfate–clay rocks do occur.

3.2. Analytical Methods and Samples Preparations

X-ray diffraction. Bulk samples were crushed in an agate mortar and pestle to pass through a 30-mesh sieve. The <2 µm clay fractions were separated at an initial clay (+sulfate)/water concentration of 10 g/L by the sedimentation method according to Stokes law, where the clay fractions were concentrated by centrifugation. No chemical treatments were used. The mineralogy of bulk samples and clay fractions was determined by X-ray diffraction (XRD) using a Rigaku Geigerflex D/max. (Rigaku Corporation, Tokyo, Japan) -C series X-ray diffractometer machine equipped with a Cu*Kα* radiation, an automatic divergence slit and a 0.5-receiving slit. X-ray diffraction of randomly samples were analyzed in the range 2–70° 2θ, with a step size of 0.05° 2θ and 5 s counting time.

Oriented clay aggregates corresponding to smectite clay fractions were X-ray run in air-dried and ethylene glycol conditions. Rich opal samples were scanned at 0.6° 2θ from 10 to 70° 2θ with a step of 0.01° [18] using a Philips X'Pert diffractometer machine. The intensity of full-width half maximum (FWHM) of the distinctive broad peak at ~4-Å attributed to opal was measured using Profile Fitting program (version 2016, Philips X'Pert ©, Philips, Amsterdam, the Netherlands). The nomenclature of the non-crystalline silica phase used is according with literature data [45–47].

Figure 2. Caldeiras-Furnas village: (**a**) boiling fumaroles with steam explosions and steam heated pools; (**b**) interaction between fumarolic acid plume and the ground surface; (**c**) acid-sulfate rocks supported changes of colours from white to yellowish and red colour caused by precipitation of FeO(OH) after the Fe^{2+} oxidation, where jarosite precipitated. Lagoa das Furnas: (**d**) Fumarole activity and steaming grounds are well spread around the Furnas lakes.

Scanning electron microscopy. Morphological study of minerals was performed using a Hitachi S-4100 scanning electron microscope (SEM) (Hitachi, Tokyo, Japan), working at 25 kV. Freshly cleaved rock chips were mounted on a carbon holder and sputter-coated with a thin carbon film.

Electron microprobe analysis. Quantitative mineral chemical compositions were obtained on doubly–polished thick sections (200 μm) of acid-sulfate samples using a Jeol Hyperprobe JXA-8500F electron microprobe (EPMA) (JEOL Ltd., Tokyo, Japan) operated at 15 kV accelerating voltage and 10 nA beam current in the case of silicates and sulfates. The intensity data were corrected with a ZAF program and detection limits (3τ) above mean background were 0.03 wt.% for most oxides with counting times of 80 s.

Chemical analysis. Samples selected from the acid-sulfate alteration for chemical analysis correspond to different mineral assemblages identified previously by XRD (Table 1). Major, trace and rare earth elements chemistry were measured on whole altered and freshly rocks by inductive-coupled plasma-mass spectrometry (ICP-MS), using Li-tetraborate procedure at ACTLab (Vancouver, BC, Canada). The REE patterns were plotted against the chondrite normalisation reference [48], in order to visualise the fractionation processes of either light- (LREE) relative to middle- (MREE) or heavy-rare earth elements (HREE) and Eu- anomaly.

Table 1. Mineral assemblages of the analysed samples by ICP-MS.

Samples	Location	Mineral Assemblages
F0	Caldeiras-Furnas	Kaolinite, alunite, opal-A
F1	Caldeiras-Furnas	Alunite, halloysite, opal-A
F2	Caldeiras-Furnas	Kaolinite, alunite ± opal-A
F3	Caldeiras-Furnas	Alunite, opal-A
F4	Caldeiras-Furnas	Opal-A, alunite
F5	Caldeiras-Furnas	Alunite, opal-A
F6	Caldeiras-Furnas	Opal-A, alunite
F7	Caldeiras-Furnas	Kaolinite, alunite
F8	Caldeiras-Furnas	Alunite, opal-A
F20	Caldeiras-Furnas	Alunite, (Feldspar)
F21	Caldeiras-Furnas	Sinter (opal-A, alunite)
F22	Caldeiras-Furnas	Sinter (opal-A, alunite)
Mud	Lagoa das Furnas	Smectite, kaolinite, alunite, (Feldspar)
Trachyte pumice	Caldeiras-Furnas	Volcanic glassy, feldspar
Trachyte	Caldeiras-Furnas	Feldspar, clinopyroxene, Fe-Ti oxides, amphibole

4. Results

4.1. X-ray Diffraction

Caldeiras-Furnas village. Trachyte products altered by acid solutions into alunite, clay and sinter rocks (caldeira das Furnas, caldeira Pero Botelho, caldeira seca) correspond to the acid-sulfate alteration. Three distinct assemblages were identified by XRD and SEM, namely: *i*) kaolinite + alunite; *ii*) alunite + opal-A ± halloysite-7Å ± native sulphur); and *iii*) opal-A ± alunite. Native orthorhombic sulphur crystals could be observed associated mainly with alunitic rocks.

X-ray pattern of randomly oriented whole kaolin rocks show kaolinite, alunite and trace amounts of quartz and feldspar (sanidine) (Figure 3a). Kaolinite occurs at 7.15 Å (001) and 3.55Å (002), K,Na-alunite at 5.68 Å, 4.90 Å, 3.49 Å and 2.96 Å, quartz at 3.33 Å and 4.21 Å and feldspar at 3.88 Å, 3.24 Å and 3.15 Å. The well-resolved triplet at 4.38 Å, 4.35 Å and 4.15 Å (020, 110 and 111) confirm a well-order kaolinite (Hinckley index = 1.14) [49]. Alunite is the main component found with halloysite-7Å and opal-A. The XRD pattern of alunite + opal-A assemblage (Figure 3b) shows the d_{hkl} reflections corresponding to alunite at 5.73 Å, 5.08 Å, 3.48 Å, 2.98 Å, 2.28 Å, 1.90 Å, 1.74 Å and 1.48 Å. The broad peak at about 4 Å corresponds to opal-A. Trace amounts of quartz was also observed at 3.33 Å.

Sinter interbeddings of 3 to 5 cm thick containing alunite + opal-A or opal-A + alunite assemblages were observed in acid-sulfate altered pumice rocks. The main component of sinters is opal-A identified by XRD, where a very broad reflection centred at about ~4 Å with a raw intensity of about 700 counts s^{-1} was observed (Figure 3c). The FWHM value corresponding to ~4 Å reflection is considered to indicate the degree of order-disorder of opal-A structure [18]. The FWHM measured is about 0.9° 2θ under the operating conditions for the samples collected.

Lagoa das Furnas. XRD pattern of the <2 μm clay fractions extracted from the mud pools show smectite, kaolinite and alunite. The XRD pattern of smectite is characterized by the d_{001} peak at 15 Å in air-dried conditions, which expanded after EG solvated at 15.9 Å (Figure 3d). A small amount of feldspar occurs in the <2 μm fractions.

Supergene alteration. Pale green and blue colour fine veins of 1 to 3 mm thick were observed in bearing rich-alunitic rocks. These fine veins correspond to melanterite ($FeSO_4·7H_2O$) precipitation, where these soluble sulfates (i.e., melanterite, etc.) represent unstable phase which stored only Fe^{2+}. The colour of these finest veins disappeared some hours later from the samples collected in plastic bags.

Also, several places were identified in the Furnas village (e.g., Calderia dos Vimes, along the Ribeira Quente brook) and *Caldeiras da Lagoa das Furnas* where the acid-sulfate rocks supported changes of colours from white to yellowish and red colour related to Fe^{2+}

oxidation and precipitation of FeO(OH). Jarosite precipitated in the supergene conditions at a low pH (<3), high Eh and sulfate available [50].

4.2. Scanning Electron Microscopy and Electron Microprobe Analysis

Scanning electron microscopy observations show well pseudoheganal plates of kaolinite sometimes with undefined plate shapes (Figure 4a), where plates varying in size (a × b) from 0.25 × 1.25 to 4 × 6.5 μm^2 (estimation carried out on 30 crystals). Kaolinite with a book-shape plates morphology wasn't observed in the samples studied. Long tubes of halloysite-7Å with lengths about 25 μm were also identified in the alunite and opal-A assemblage (Figure 4b). Alunite crystals display either pseudo-cubic or rhomboidal habit (Figure 4c,d). Coalesced aggregates of opal-A exhibit a lepisphere shape (Figure 4e). Finally, pumices exhibit evident devitrification processes origining embryonic opal lepisphere (Figure 4f), where successive coalesced of small lepispheres show the overgrowths in a gel-like texture. Kaolinite, alunite and feldspar were analyzed by EPMA (Table 2). Kaolinite (normalization at 14 oxygen atoms) contains only Si and Al in tetrahedral and octahedral sheets. Alunite (normalization at 14 oxygen atoms) contains both K^+ and Na^+ fixed cations in different proportions beside Al^{3+} and SO_2. Undissolved feldspar (normalization at 8 oxygen atoms) found in acid-sulfate rocks shows a mean normative composition of $An_4Ab_{58.2}Or_{37.8}$ (Table 2) which it lies at the orthoclase-sanidine boundary in the ternary diagram of An–Ab–Or system (not shown).

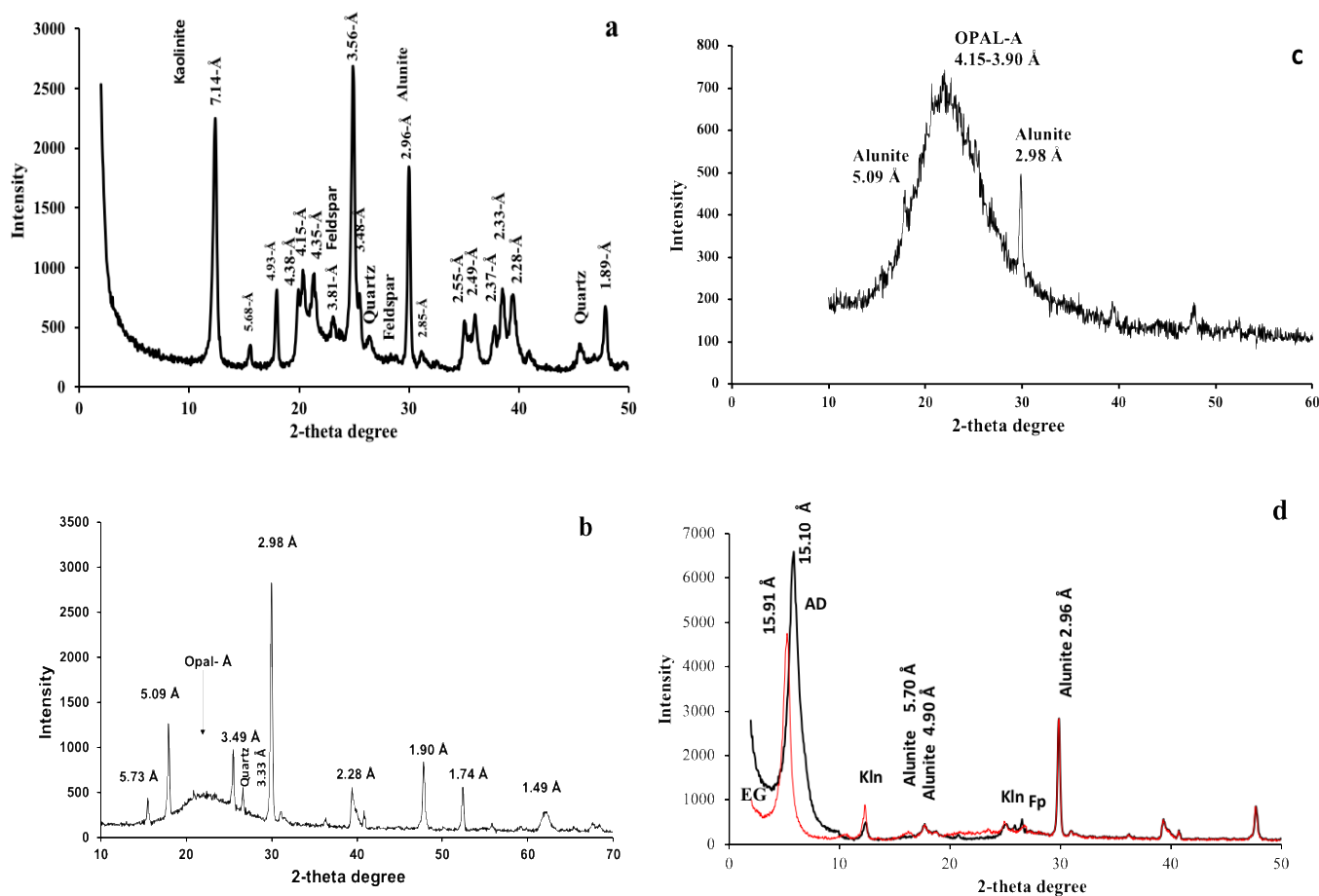**Figure 3.** XRD patterns of randomly oriented aggregates: (**a**) kaolinite − alunite assemblage (quartz and K-feldspar traces); (**b**) alunite − opal-A assemblage; (**c**) sinter constituted by opal-A + alunite assemblage. (**d**) XRD pattern of oriented clay aggregates (<2 μm clay fractions, sample Mud clays) of smectite + kaolinite + alunite assemblage. AD: air-dried; EG: ethylene glycol.
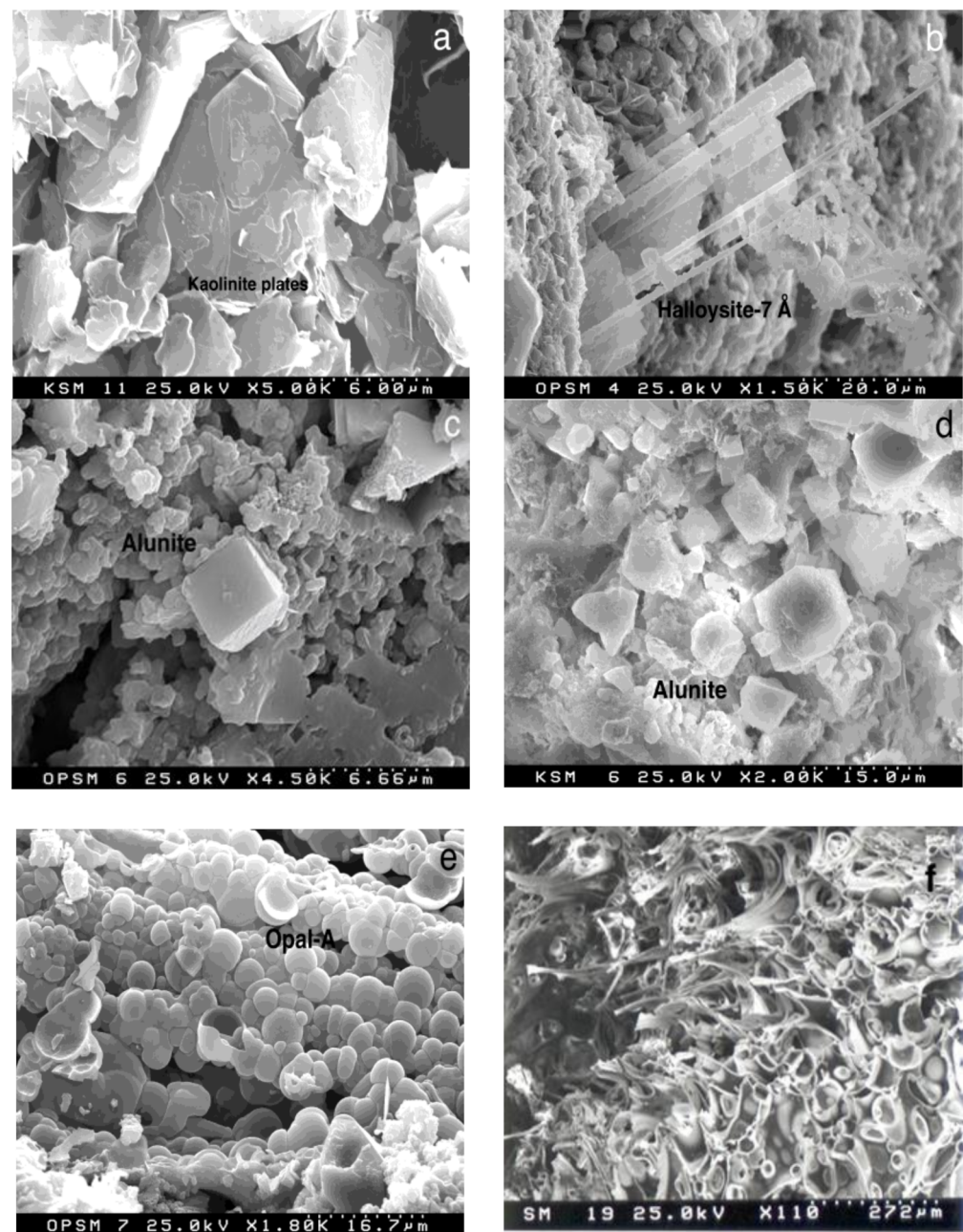
Table 2. Electron microprobe analysis of sanidine, alunite and kaolinite (n: number of analyses).

Oxides	Feldspar *n* = 5	Feldspar *n* = 5	Feldspar *n* = 5	Feldspar *n* = 5	Feldspar *n* = 5	Feldspar *n* = 5	Feldspar *n* = 5	Alunite *n* = 5	Alunite *n* = 5	Alunite *n* = 5	Alunite *n* = 5	Alunite *n* = 5	Kaolinite *n* = 5	Kaolinite *n* = 5	Kaolinite *n* =5
SiO_2	67.63	65.78	65.58	65.97	65.95	66.02	65.28	0.2	0.35	0.56	0.10	0.16	45.24	44.15	45.2
TiO_2	0.28	0.12	0.14	0.19	0.15	0.14	0.11	0.00	0.00	0.00	0.00	0.00	0.00	0.02	0.00
Al_2O_3	20.69	21.35	21.07	20.59	20.09	20.66	20.71	48.35	52.35	49.28	49.59	50.14	37.98	38.29	38.37
FeO	0.53	0.31	0.34	0.35	0.37	0.32	0.22	0.01	0.02	0.06	0.05	0.03	0.19	0.06	0.11
MnO	0.00	0.00	0.02	0.00	0.02	0.00	0.00	0.00	0.00	0.00	0.00	0.00	0.00	0.00	0.00
MgO	0.00	0.00	0.00	0.00	0.00	0.00	0.00	0.00	0.00	0.00	0.00	0.00	0.00	0.00	0.00
CaO	0.40	1.17	1.04	0.59	0.28	0.75	0.99	0.03	0.01	0.03	0.01	0.01	0.00	0.00	0.00
Na_2O	4.54	6.28	6.15	5.91	5.75	6.30	5.55	0.77	0.21	0.56	0.23	0.34	0.00	0.00	0.00
K_2O	6.39	4.30	5.48	6.09	7.71	6.21	7.42	2.1	2	2.54	2.36	2.44	0.00	0.00	0.00
SO2	0.00	0.00	0.00	0.00	0.00	0.00	0.00	34.89	35.32	35.32	36.51	35.82	0.00	0.00	0.00
Total	100.47	99.32	99.81	99.68	100.32	100.41	100.29	86.35	90.26	88.34	88.86	88.94	83,41	83.47	83.68
Si	2.979	2.926	2.923	2.946	2.952	2.955	2.922	0.00	0.01	0.02	0.00	0.0	1.99	1.97	1.98
Ti	0.009	0.004	0.005	0.006	0.005	0.005	0.004	0.00	0.00	0.00	0.00	0.00	0.00	0.00	0.00
Al	1.074	1.119	1.107	1.084	1.059	1.090	1.092	1.76	1.82	1.76	1.75	1.75	1.97	2.01	2.01
Fe	0.020	0.012	0.013	0.013	0.014	0.012	0.008	0.00	0.00	0.00	0.00	0.00	0.00	0.00	0.00
Mn	0.000	0.000	0.001	0.000	0.001	0.000	0.000	0.00	0.00	0.00	0.00	0.00	0.00	0.00	0.00
Mg	0.000	0.000	0.000	0.000	0.000	0.000	0.000	0.00	0.00	0.00	0.00	0.00	0.00	0.00	0.00
Ca	0.019	0.056	0.050	0.028	0.013	0.036	0.048	0.00	0.00	0.00	0.00	0.00	0.00	0.00	0.00
Na	0.388	0.542	0.532	0.512	0.499	0.547	0.482	0.05	0.12	0.03	0.01	0.02	0.00	0.00	0.00
K	0.359	0.244	0.312	0.347	0.440	0.355	0.424	0.08	0.08	0.1	0.09	0.09	0.00	0.00	0.00
S	0.000	0.000	0.000	0.000	0.000	0.000	0.000	0.95	0.88	0.91	0.93	0.92	0.00	0.00	0.00
Total	4.848	4.903	4.941	4.935	4.983	4.999	4.979	2.83	2.91	2.73	2.78	2.78	3.96	3.98	3.99
An	2.5	6.6	5.6	3.2	1.4	3.9	5.0								
Ab	50.6	64.4	59.5	57.7	52.4	58.3	50.6								
Or	46.9	29.0	34.9	39.1	46.2	37.8	44.4								
Total	100.0	100.0	100.0	100.0	100.0	100.0	100.0								

Figure 4. Scanning electron microscope images of kaolinite plates (**a**), halloysite-7Å tubes (**b**), alunite crystals (**c**,**d**), opal-A lepisphere (**e**) and volcanic glass dissolved in trachyte pumice rocks with embryonic opal-A formation (**f**).

4.3. HFSE and REE Geochemistry

Trace and rare earth elements were measured on altered and freshly trachyte rocks (Table 3) from the Furnas craterial volcanic area. Concentrations of lithophile (Cr, U, Rb, Cs), siderophile (Co, Ni, W) and chalcophile (Cu, Pb, Zn, As, Ga, Sn) elements show values close to those values measured in fresh rocks.

High-field-strain elements measured in altered acid-sulfate sulfate rocks show high concentrations with respect to fresh trachyte rocks, being reliable geochemical indicators own to their immobility in most geological settings. Nevertheless, there is clear evidences which suggested their mobility in fluid-driven systems due to the influence of halogens, e.g., chlorine and fluorine [51,52]. High amounts of Nb (78.77 to 623.8 ppm), Zr (424.6 to 3192.5 ppm), Hf (9.8 to 70 ppm) and Y (9.4 to 53.9 ppm) were identified in acid-sulfate rocks,

where mud samples contain higher concentrations than clay-sulfate or sinter rocks. The Nb vs. Ta and Zr vs. Hf diagrams (Figure 5a,b) show a large fractionation and a positive correlation with a good correlation coefficient. The Nb/Ta ratio (17.90 to 23.75) is slightly higher than in fresh rocks (15.34 and 23.01). Also, Zr/Hf ratio shows a weak fractionation from 41.23 to 45.60 with respect to fresh rocks (49.71 to 65.52). Both Nb/Ta vs. Zr/Hf ratios (Figure 5c) show lower values in acid sulfate rocks than those obtained for fresh rocks, confirming a fractionation of Nb, Ta, Zr and Hf. In addition, the continental crust has a lower Nb/Ta ratio (= 12 to 13) than the bulk silicate Earth (Nb/Ta = 1470.3; [53]).
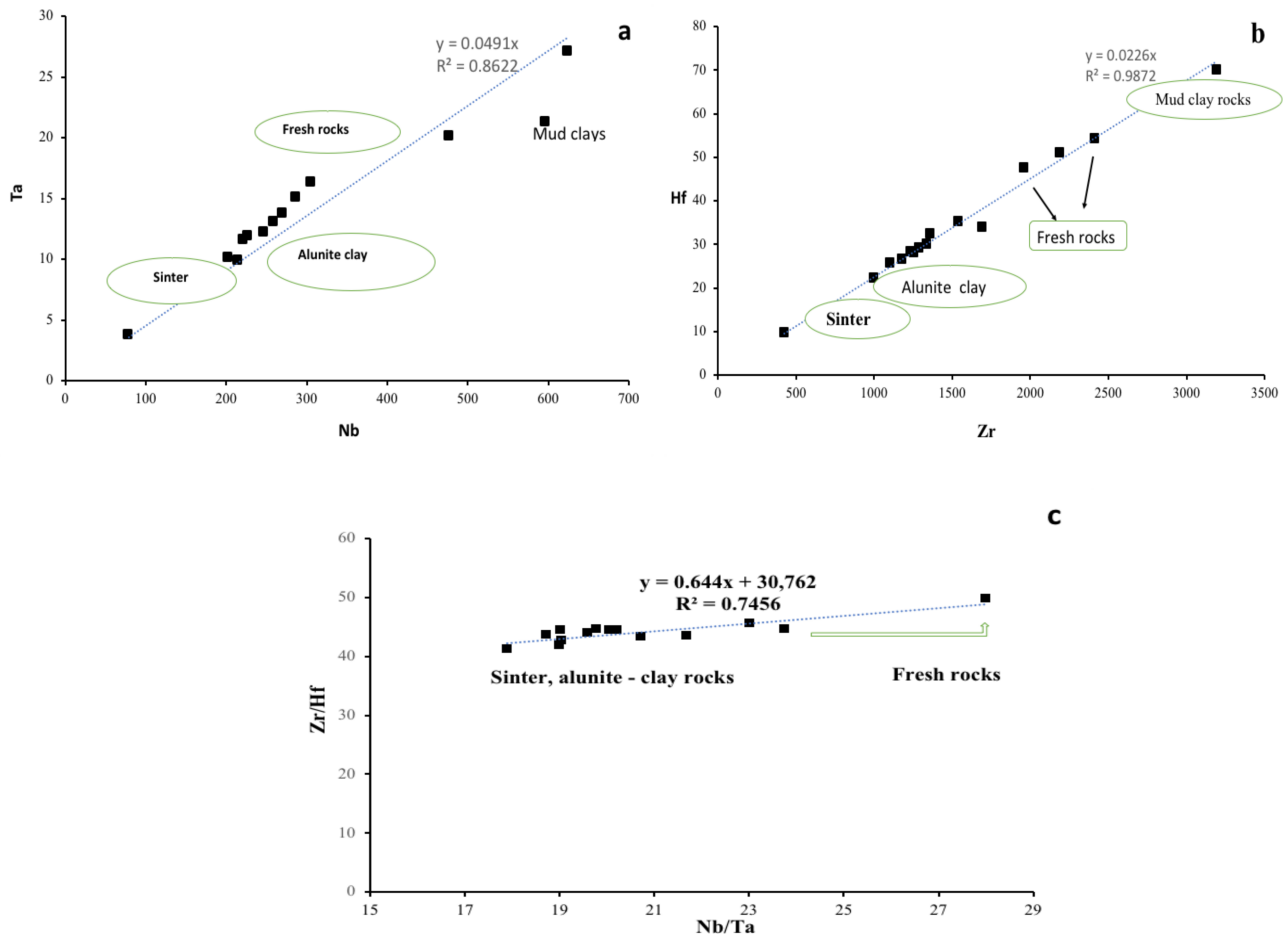
Figure 5. The diagram of Nb vs. Ta (**a**), Zr vs. Hf (**b**) and Nb/Ta vs. Zr/Hf (**c**) corresponding to sinter, alunite-clay and fresh rocks.

Table 3. Trace elements concentration (ppm) of the analyzed samples.

Samples	Cu	Pb	Zn	As	Ba	Ni	Cr	Co	Cs	Ga	Hf	Nb	Rb	Sn	Sr	Ta	Th	Tl	U	V	W	Zr	Y
Fo	9	11	34	5	247.5	11	6	0.4	0.6	47.8	30	259.21	44.14	8	176.9	13.1	25.6	0.2	4.2	43	4.1	1336.3	26.1
F1	11	8	17	5	119.9	15	5	0.6	0.8	39.8	47.5	361.69	23.87	12	68.2	20.2	24.1	0.5	7.6	25	8.7	1958.6	33.4
F2	3	4	4	5	294.4	9	4	0.3	0.6	50.2	35.2	305.38	25.87	10	207	16.3	25.3	0.4	5.3	30	5.6	1537	27.1
F3	5	8	6	5	211.1	13	8	0.6	0.6	43.2	25.8	226.8	24.52	10	140.7	11.9	12.2	0.6	4	23	3.6	1101.1	14.3
F4	4	6	4	5	211.8	9	5	0.6	0.6	39.6	32.5	287.02	25.55	8	113.3	15.1	11	0.4	4.6	24	4	1359.7	10
F5	2	7	5	5	104	16	11	0.5	0.7	31.8	28.2	220.74	17.96	5	64.3	11.6	13.3	0.2	2.6	17	2.6	1254.8	9.4
F6	2	4	3	5	182.1	12	3	0.4	0.4	35	26.6	246.8	22.72	8	117.4	12.2	13.2	0.4	2.9	13	4.1	1179.7	13.3
F7	9	12	7	5	282	8	12	0.5	0.2	89.6	54.2	477.45	9.71	10	224.5	20.1	29.3	0.2	4.3	16	7.6	2414.4	35.6
F8	4	5	2	5	169.1	10	7	3.5	0.8	28.5	22.4	202.58	19.41	7	85.9	10.1	19.9	0.3	7.3	21	3.3	996.1	31.9
F20	5	3	23	5	24.3	5	4	0.3	1.9	37.9	29.3	270.5	218.64	8	11.1	13.8	23.6	0.1	7.3	10	4	1285.2	70
F21	3	4	2	5	310.2	11	8	0.4	0.8	10.2	28.4	214.7	29.36	5	50.3	9.9	9.4	0.2	2.7	23	4.3	1235.3	12.9
F22	1	3	74	5	279.5	9	5	1.5	0.4	28.7	9.8	78.77	117.48	3	85.7	3.8	7.7	0.1	2.3	20	0.5	424.6	21.5
Mud	3	3	8	5	360.6	14	6	0.4	0.4	84.2	70	623.8	17.72	11	184.4	27.1	32.8	0.2	5.6	34	8.5	3192.5	53.9
Trachyte pumice	4	11	66	5	169.1	4	3	1.8	2.1	112.8	34	326.75	221.32	9	126.52	21.3	34	0.6	7.8	38	5.1	1690.26	74
Trachyte	6	9	82	5	286.3	8	6	1	0.9	94.7	51	391.56	263.98	6	148.31	27.5	41	0.9	6.3	59	7.4	2189	112

The REE chondrite normalized [48] patterns corresponding to sulfate − kaolin minerals ± opal-A (alunite − clay rocks), opal-A ± sulfate (sinter) and smectite + kaolinite ± alunite (mud) assemblages were compared with those of fresh trachyte rocks (Table 4). Chondrite-normalized REE patterns of selected samples (Figure 6) display a gull-wing shapes [54] where water-rock interaction process plays a significant role in this shape-type formation [55]. The Eu negative anomaly (the gull body) and light (La/Sm) and heavy (Gd-Lu) "wings" suggest an association with an acid-sulfate systems observed elsewhere (i.e., Taupo, Vulcano, etc) [56,57].

Table 4. Rare earth elements concentration (ppm) of the analyzed samples.

Samples	La	Ce	Pr	Nd	Sm	Eu	Gd	Tb	Dy	Ho	Er	Tm	Yb	Lu	Y
F0	245.2	473.2	44.87	132.2	14.5	0.99	8.01	1.03	6.11	1.06	3.16	0.47	3.2	0.5	26.1
F1	132.3	262.8	27.71	85.3	11.6	1.02	7.19	1.14	7.06	1.39	3.98	0.59	3.99	0.58	33.4
F2	235.4	409.6	39.66	131.1	18	1.24	9.37	1.21	6.68	1.14	3.33	0.44	3.03	0.47	27.1
F3	114.6	178.2	16.58	57.8	8.7	0.55	5.28	0.63	3.6	0.56	1.62	0.23	1.5	0.23	14.3
F4	88.1	123.4	10.63	33.2	5	0.38	2.7	0.4	2.19	0.39	1.18	0.16	1.04	0.16	10
F5	122	192.1	16.33	48.4	6.9	0.46	3.13	0.44	2.72	0.38	1.1	0.16	1.15	0.15	9.4
F6	139.9	201.2	17.31	53.6	7.4	0.56	4.11	0.52	3.19	0.54	1.46	0.2	1.29	0.21	13.3
F7	279.2	357.7	27.15	76.7	10.8	0.85	6.4	1.07	6.75	1.37	4.17	0.61	3.86	0.64	35.6
F8	148.5	242.2	18.15	37.5	4.6	0.58	4.71	0.79	5.55	1.12	3.44	0.5	3.18	0.49	31.9
F20	184.2	345.4	35.03	123.8	20.5	0.92	14.61	2.24	14.16	2.61	7.26	1.07	5.98	0.94	70
F21	45.7	79.9	7.37	23.1	3.7	0.4	2.32	0.36	2.51	0.47	1.4	0.21	1.4	0.21	12.9
F22	48.4	148.3	11.92	47.6	8.8	1.9	6.16	0.84	4.96	0.86	2.32	0.32	1.95	0.33	21.5
Mud	276.1	376.5	29.69	82.1	11.6	0.94	7.49	1.35	9.3	1.87	5.92	0.96	5.98	0.93	53.9
Trachyte	146	232	28.3	101	17	1.79	12	1.8	11	2.3	6.4	0.85	4.6	0.62	74
Trachyte pumice	178.6	346.1	37.43	119.82	18.77	0.61	15.89	2.33	13.81	2.55	7.11	0.91	6.34	0.93	112
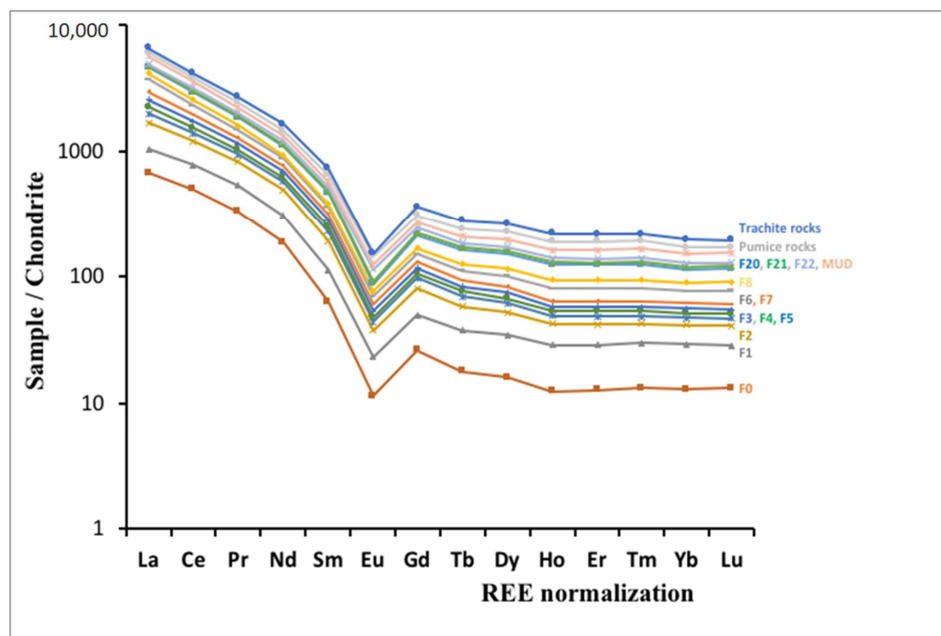
Figure 6. The REE chondrite normalization patterns of sinter, alunite-clay and fresh rocks.

The ∑REE (Table 5) ranges from 169.05 to 934.5 ppm in acid-sulfate rocks, values higher than those found in trachyte rocks (565.66 and 751.2 ppm). Higher ∑REE concentrations (from 431.49 to 934.5 ppm) contain kaolin − alunite and smectite + kaolin + alunite assemblages. The REE uptake into the sinter rocks (169.05 to 268.93 ppm) is of 2 to 4 orders magnitude lower than in alunite + kaolin assemblage. In addition, a high LREE (156.07 to 895.47 ppm) fractionation compared with HREE (2.54 to 15.25 ppm) characterizes the selected samples. The (LREE/HREE)$_N$ ranges from 4.22 to 18.36 in acid-sulfate rocks comparatively with fresh rocks (12.47 and 12.39). The Eu/Eu* anomaly (Table 5) is very

large ranging from 0.16 to 0.78 in acid-sulfate rocks (including sinter and muds). The Eu depletion in whole acid-sulfate rocks compared with unaltered rocks, imply a dissolution of sanidine mineral and glass during acid sulfate alteration of trachyte (Eu/Eu* = 0.38) and trachyte pumice (Eu/Eu* = 0.10) rocks. Higher Ce/Ce* ratio values (Table 5) from 0.94 to 1.45 were found in acid-sulfate rocks than in fresh volcanic rocks (0.84 to 0.99). In the case of a possible positive Gd anomaly, the interpolation occurs between Sm and Tb, where the Eu shows a negative anomaly. However, the Gd/Gd* [Gd/Gd* = Gd*/(0.33Sm$_N$ + 0.67Tb$_N$)] calculated ratio is <1 (Table 5), which means no positive anomaly [58].

The (La/Sm)$_N$ and (La/Yb)$_N$ ratios (Table 5) of acid sulfate rocks show two distinct vectors with a large fractionation observed in the (La/Sm)$_N$ vs. (La/Yb)$_N$ diagram (Figure 7). The (La/Sm)$_N$ ratio is well fractionated in alunite-opal-A and mud assemblages, whereas the (La(Yb)$_N$ in kaolinite + alunite ± opal-A assemblage. Also, the wide range of (La/Ce)$_N$ ratio (1.31 to 2.03) reflects pronounced fractionation of La during acid sulfate alteration.
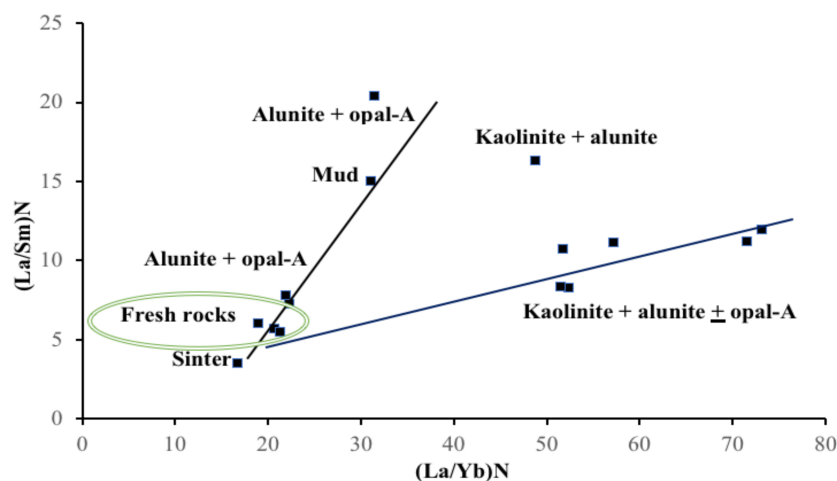
Figure 7. The diagram of (La/Yb)$_N$ vs. (La/Sm)$_N$.

A strongly depletion of MREE (55.04 to 9.76) and HREE (15.25 to 2.54) show the acid-sulfate rocks comparatively with fresh trachyte (53.96 to 45.89) and trachyte pumice rocks (15.29 to 12.47), respectively. As we expected, the (Tb/Yb)$_N$ ratio shows a large fractionation from 0.96 to 1.84 in acid-sulfate rocks relatively to fresh rocks (1.67 to 1.57) (Table 5) and no (Tb/Lu)$_N$ fractionation was observed.

Yttrium(III) content, considered often an analog of HREE due to the fact of having radius close to Dy(III) or Ho(III), ranges from 9.4 to 53.9 ppm in acid sulfate rocks (Table 5). Y and HREE become fractionated in aqueous systems, resulting in non-chondritic Y/Dy and Y/Ho ratios [59]. The Y/Dy ratio shows a large fractionation from 3.45 to 5.79 in acid-sulfate rocks with respect to fresh rocks (6.72 and 8.11). Also, Y/Ho ratio ranges from 23.77 to 28.48 (in fresh rocks from 28.82 to 32.17). The data plotted in the Y vs. Dy and Y vs. Ho diagrams (Figure 8a,b) show a very good positive correlation coefficient, where Y and Dy(Ho) are large fractionated in acid-sulfate rocks with respect to fresh rocks. The Y/Dy and Y/Ho ratios (Figure 8c) show a lower ratio and a weak fractionation with a low correlation coefficient with respect to fresh rocks.

Table 5. Sum of the REE concentrations and REE chondrite normalized ratios.

Samples	SUMREE	LREE	HREE	MREE	(LREE/HRRE)$_N$	(La/Yb)$_N$	(La/Ce)$_N$	Ce/Ce*	Eu/Eu*	(La/Sm)$_N$	(Tb/Yb)$_N$	(Gd/Gd)$_N$	Y/Ho	Y/Dy
Fo	934.50	895.47	7.33	31.7	18.36	51.78	1.35	1.06	0.28	10.64	1.38	0.80	24.62	4.27
F1	546.65	508.11	9.14	29.4	9.46	22.41	1.31	1.02	0.34	7.18	1.22	0.79	24.03	4.73
F2	860.67	815.76	7.27	37.64	17.06	52.50	1.49	0.99	0.29	8.23	1.71	0.77	23.77	4.057
F3	390.08	367.18	3.58	19.32	9.80	51.63	1.67	0.96	0.25	8.29	1.79	0.87	25.53	3.97
F4	268.93	255.33	2.54	11.06	7.48	57.24	1.86	0.94	0.32	11.09	1.64	0.75	25.64	4.56
F5	395.42	378.83	2.56	14.03	10.91	71.68	1.65	1.01	0.30	11.13	1.64	0.68	24.74	3.46
F6	431.49	412.01	3.16	16.32	11.47	73.28	1.81	0.96	0.31	11.90	1.72	0.81	24.63	4.17
F7	777.27	740.75	9.28	27.24	14.13	48.88	2.03	0.96	0.31	16.27	1.18	0.75	25.98	5.27
F8	471.31	446.35	7.61	17.35	9.05	31.56	1.59	1.09	0.38	20.32	1.06	0.98	28.48	5.75
F20	758.72	688.43	15.25	55.04	9.52	20.81	1.39	1.01	0.16	5.65	1.60	0.86	26.82	4.94
F21	169.05	156.07	3.22	9.76	4.22	22.06	1.49	1.02	0.42	7.77	1.09	0.80	27.45	5.14
F22	284.66	256.22	4.92	23.52	5.60	16.77	0.85	1.45	0.79	3.46	1.84	0.90	25	4.33
Mud	810.73	764.39	13.79	32.55	11.60	31.20	1.912	0.97	0.31	14.98	0.96	0.76	28.82	5.79
Trachyte	565.66	507.3	12.47	45.89	11.72	21.45	1.64	0.84	0.38	5.40	1.67	0.87	32.17	6.73
Trachyte pumice	751.2	681.95	15.29	53.96	12.39	19.04	1.34	0.99	0.11	5.99	1.57	0.96	43.92	8.11
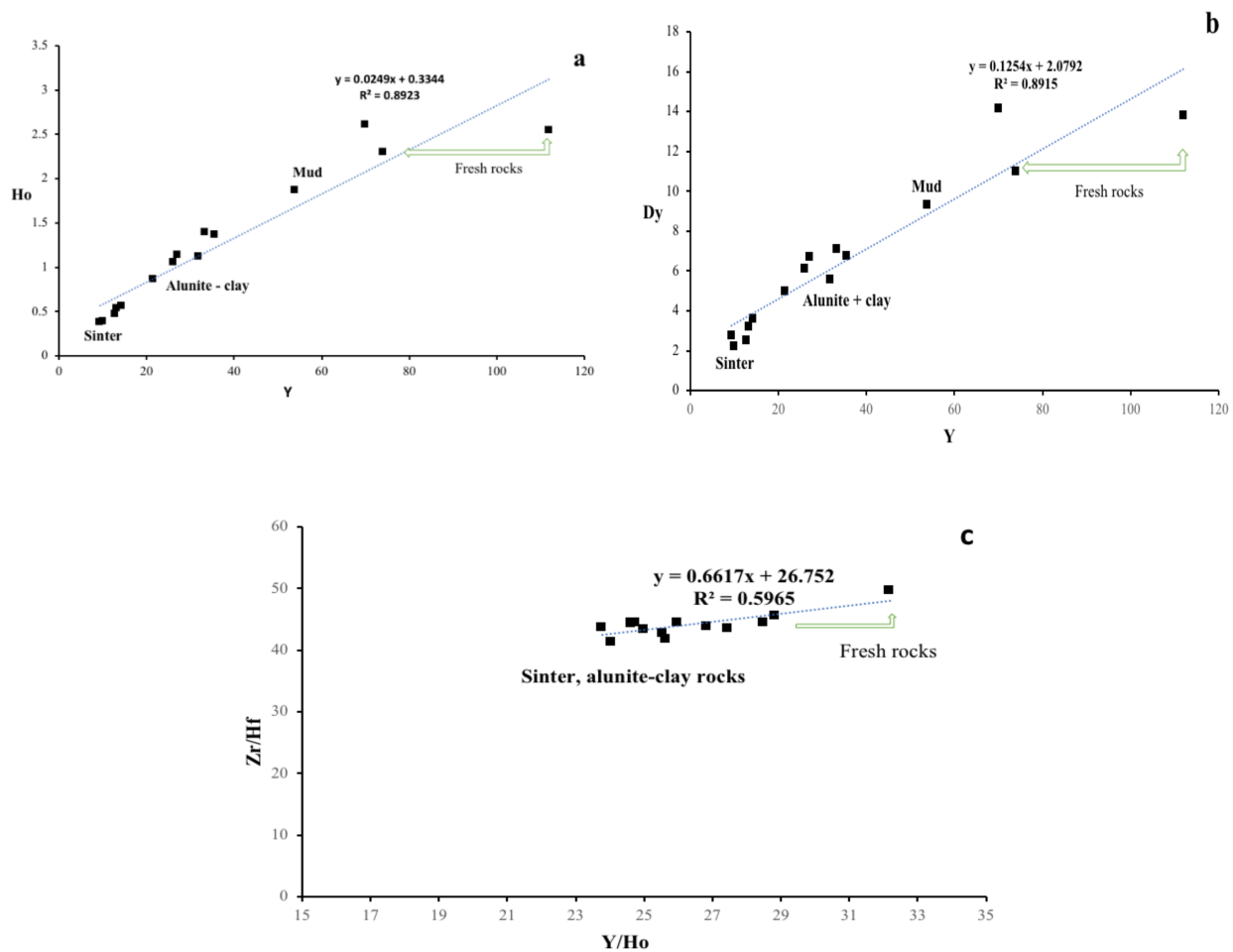
Figure 8. The diagram of Y vs. Ho (**a**), Y vs. Dy (**b**) and Y/Ho vs. Zr/Hf (**c**) corresponding to sinter, alunite-clay and fresh rocks.

5. Discussion

Mineralogy. The thermal water rising to the surface in hot springs is entirely meteoric water heated–up by vapours emanating from the magma chamber. The acidity of the fumarole and thermal springs is a consequence of H_2S and S oxidation with production of H_2SO_4 at low temperature (below 200 °C) in a convective meteoric system. The acid-sulfate meteoric fluid circulation in a volcanic or post-volcanic environment interacted with the minerals from trachyte rocks, generating a suite of neoformation minerals that represents a high potential for REE concentrations in geothermal waters. Sulphuric acid production during sulphur oxidation dissolved silicates from host rocks producing clays, muds, sulfates and sinter.

Acid-sulfate alteration in the Furnas area is comprised by clays, sulfate, sinter and native sulphur minerals crystallized as neoformation products from dissolution of primary minerals during water-rock interaction at temperatures around 100–150 °C [30]. Kaolinite and halloysite-7Å crystallization is a function of the degree of solution supersaturation within a pH ~3. The kaolinite shape morphology observed in acid-sulfate alteration from the Furnas area is different than the morphology observed during kaolinite formation from mica or feldspar in granitic rocks [60,61]. Halloysite-7Å was found associated always within the alunite + opal-A assemblage, whereas well-ordered kaolinite occurs either as single mineral phase in the <2 μm fraction or in assemblage with alunite, quartz or smectite.

Quartz resulted as a by-product during kaolinite precipitation. Also, in weathered trachyte pumice rocks occur halloysite-10Å [62].

Smectite occurs in steamy grounds near the Furnas lake in assemblage with kaolinite (halloysite-7Å) + alunite, representing a mechanical mixture between two alteration types. This means that smectite crystallized under different conditions related to an older crystallisation event imposed by a propylitic stage than by the present-day hot fluid circulations which generated acid-sulfate clay. Smectite crystallized from glassy dissolution of trachyte pumice rocks rather than feldspar, where the reaction of smectite formation depends on glass chemical composition, the fluid pH and fluid/rock ratio [63–65]. Nevertheless, smectite does not discard to other environment at high temperature [66] or lower pH at the end of an acid-sulfate alteration, when pH could be neutralized [67].

In a sulfate-rich system, alunite forms when H^+ activity decreases and both K^+/Na^+ and SO_4^- activities increase. Alkali-ion concentrations might rise to high values to stabilise alunite formation. From subsequent oxidation of H_2S at the surface of the alteration zone native sulphur crystalizes. Native sulphur is one of the last mineral which precipitate in a sulfate-rich system related to a post-volcanic activity, being a common mineral found also in other active hydrothermal systems [24,68,69]. Also, the sulfuric acid is produced by hot springs due to near surface oxidation of effluent S-bearing gases close to ~95 °C in an environment with a pH at 4.5 [70].

Interbeds of sinter were deposited at the surface as the result of silica excess polymerised forming a colloidal suspension that subsequently produced opal. Otherway, silica may forms complexes with sulfate, where the excess of high-silica supersaturation may precipitate in the acid environment, as sulfate is removed from solution forming alunite.

During supergene alteration, the oxidation reaction rates of Fe^{2+} into Fe^{3+} increased either due to microbial activity or oxygen from air or water conditions ($Fe^{2+} + 1/4O_2 + H^+ = Fe^{3+} + 1/2H_2O$). The hydrolysis and precipitation of FeO(OH) will produce more acidity in this process. If pH is less than about 3.5, Fe(OH)3 is not stable and Fe^{3+} remains in solution [$Fe^{3+} + 3 H_2O = Fe(OH)_3(s) + 3H^+$]. Jarosite is generally formed at oxidizing low-pH conditions (pH < 3) being the first phase precipitating subsequently to alunite formation during hydrothermal conditions. Jarosite formation is limited by the availability of K or Na deriving from feldspar alteration in a more acidic micro-environment [71], being disseminated in the oxidation zone outer of fumarole and hot springs areas. Melanterite is one of the first simple sulfates precipitated in the high SO_4^{2-} concentration in extreme low pH, especially in acid mine drainage environments where it promotes the speciation of Me^{n+} with SO_4^{2-} [72,73]. The dehydration process of melanterite is accompanied by its dissolution, generating acid production upon dissolution and hydrolysis [74].

High field strength elements. The HFSE can be transported by a variety of fluids under magmatic, metamorphic and hydrothermal environments. Consequently they are also used as tracers to distinguish the protoliths of altered rocks based on its "conservative" nature [75]. The Nb, Ta and Zr have significantly higher concentrations in hydrothermal altered rocks as compared to fresh rocks. The geochemical behaviour of Nb and Ta is intimately linked to that of the more abundant titanium in oxide minerals. Thus, the dominant mineral hosts of Ti, Nb and Ta in crustal rocks are Fe-Ti oxides such as: rutile, ilmenite and Ti-magnetite. Both Ti-magnetite and ilmenite occur in the trachyte rocks (sub-Plinian eruption) of the UFG [37], where the Nb and Ta budget was stored in these minerals during magmatic crystallization. However, both Nb and Ta are insoluble at low temperatures, remaining to be incorporated probably into hydrothermal rutile formed after oxidation of Fe-Ti-oxides.

The Nb vs. Ta and Zr vs. Hf diagrams (Figure 5a,b) display a positive correlation trend and a widely scattered positive relationships suggesting a large fractionation during acid-sulfate alteration. Otherwise, the Nb/Ta and Zr/Hf ratios (Figure 5c) remained rather constant with lower values than to fresh rocks, confirming a fractionation in an acid low-temperature environment fraction.

No secondary Zr- or Hf-minerals were reported after dissolution of primary and accessory silicates in acid-sulfate rocks altered. However, the breakdown of sodic pyroxene and amphibole released Zr to the hydrothermal fluids, resulting in a gain of Zr in the hydrothermally altered rocks [76]. The presence of SO_4 complexes in hydrothermal systems could facilitate the transport of Zr and Hf under acidic and oxidizing conditions, where dominating Zr species are hydroxides such as $Zr(OH)_n$ [77].

Rare earth elements. The REE geochemistry of acid-sulfate alteration provide information concerning the water-rock reaction, where the relative abundances of REE in solid phases depend upon the temperature, fluid chemistry and the nature of neoformation phases [78,79].

Glassy matrix from pumice rocks and feldspar (sanidine), pyroxene and amphibole from trachyte rocks are the main sources of REE during cold water/rocks interaction. Higher temperature and lower pH caused dissolution of glassy and minerals in the host rocks, making to increase the REE concentration as pH decreased.

The REE chondrite normalized patterns of acid-sulfate samples inherited the trend of trachyte rocks, where the chondrite normalization is revealed by Eu depletion. Also, a chondrite-normalized REE pattern similar to the "gull-wing" trend shows the host rocks, where the less Eu-rich feldspar during cold water–rocks interaction is well highlighted in all neoformation products related to acid-sulfate envelope. The REE pattern of acid-sulfate rocks is dominated by the REE trend of whole fresh rocks.

Higher $\sum$REE amounts (up to 934.5 ppm) were found in clay-sulfate assemblages and lower $\sum$REE amounts in sinter (opal-A $\pm$ sulfate, 169.05 ppm) than to fresh rocks (up to 751.2 ppm). The total concentration of dissolved REE in waters (fumaroles and boiling pools) from the São Miguel island ranges between 8.0 and 3169 nmol L$^-$ [44], reflecting a near congruent dissolution of trachyte rocks.

The clay-sulfate samples show an enrichment in LREE and a higher $(LREE/HREE)_N$ ratio (up to 18.35), suggesting a very large fractionation across to REE series. By contrast, the opal-A $\pm$ sulfate (sinter) assemblage has a lower $(LREE/HREE)_N$ ratio at about 4.22. Opposing to hydrated silica, lower amounts of REE are incorporated in quartz [80]. The fluid pH had controlled the take-up of REE into sinter (390.08 ppm) or mud rocks (934.5 ppm). Furthermore, Woitischek [43] identified a high LREE depletion vs. HREE in boiling pools waters (sodium bicarbonate waters, Furnas area) characterized by lower pH and higher SO_4 contents explained by the alunite precipitation.

The Eu/Eu* shows a large fractionation of acid sulfate rocks from 0.16 to 0.78 with respect to fresh trachyte rocks (0.10 to 0.38), indicating a negative Eu anomaly. Also, a negative Eu anomaly (0.13 to 0.60) was found in waters [43] that leached the trachytic rocks (Eu/Eu* = 0.15 and 0.56) from the Furnas area. The presence of the Eu anomaly can be used as a water-rock interaction proxy reflecting the dominance of trachyte leaching in the present case [81].

The pronounced negative Eu anomaly trend is interpreted as a partial degree of feldspar alteration leading to lower Eu content. In fact, Eu is fractionated during fluid-rock interaction under suitable conditions of oxygen fugacity, temperature and pH as a consequence of Eu^{3+} to Eu^{2+} changes allowing to Eu^{2+} to form hydroxide complexes more stable than Eu^{3+} [82,83].

The LREE enrichments and positive Eu anomaly [84] imply the dissolved REE complexes, REE mobility and fractionation induced during the secondary mineral crystallization. Also, a positive Eu anomaly in low pH sulfate-rich hydrothermal fluids from Yellowstone was reported [85], suggesting a preferential breakdown of Eu-rich sanidine.

Variation of $(La/Sm)_N$ and $(La/Yb)_N$ ratio show a larger fractionation during the acid-sulfate alteration compared to fresh trachyte rocks, where two distinct trends are observed. One from fresh rocks and sinter to mud and alunite + opal-A and the second, towards kaolin + alunite $\pm$ opal-A. The $(La/Sm)_N$ ratio ranges from 3.46 to 20.31 (fresh rocks from 5.40 to 5.99) and $(La/Yb)_N$ ratio from 16.77 to 73.28 (fresh trachyte rocks 21.44 to 19.03). This means a large fractionation of $(La(Sm)_N$ in sinter, mud and alunite + opal-A and

a large fractionation of $(La/Yb)_N$ in kaolin + alunite rocks. In addition, a large fractionation of $(La/Ce)_N$ ratio from 0.85 to 1.91 of acid-sulfate rocks than fresh rocks (1.64 to 1.32) was also observed.

Yttrium amount measured reflects the REE abundances and mobility in acid-sulfate rocks. In fact, Y and Ho or Dy fractionation (with similarly charged and sized) is observed during the precipitation of alunite and clays where a positive correlation was highlighted (Figure 8). This means that during acid-sulfate alteration process the non-chondritic Y and Ho or Dy remained tightly coupled towards sinter formation where lower amounts were found. Furthermore, non-chondritic Y/Dy and Y/Ho ratios of acid sulfate rocks remained constant with lower values than the fresh rocks, providing a good evidences for Y vs. Ho(Dy) fractionation in low temperature.

HFSE show a large fractionation during acid-sulfate alteration stage and the REE concentrations increased in acid-sulfate rocks from the convective hydrothermal system of Furnas. The REE were released from primary minerals (i.e., feldspars), sorbed by sulfate complexes and taken up by the alunite and clays. The relative proportions of Ln^{3+} and $LnSO_4$ species are related to pH and the type of crystal-chemistry of the sulfate precipitated [86]. REE adsorption onto kaolinite surfaces shows a clear pH dependence, where dominant electrostatic interaction and specific site binding due to the negatively charged kaolinite surface occur at low pH from 3 to 4 (needed for kaolin formation) which enhanced the REE adsorption [87,88].

Acid-sulfate alteration model. The alteration of primary minerals and direct precipitation from oversaturated solutions in active geothermal fields depends of temperature, composition and pH of solutions, fluid/rock ratio, where several clay formation episodes may be recorded in the same rock.

The acid-sulfate alteration model (Figure 9) proposed for the Furnas area is based on the classical model [89], where the distribution of isotherms above the heat source is influenced by the convective system recharged by meteoric or/and sea waters. Isotopic ($\delta^{18}O_{H2O} = -3.3$ ‰ and $\delta D_{H2O} = -16.9$‰) composition of the discharged waters (spring and boiling pools) from the Furnas correspond to meteoric water or mixture of seawater and meteoric water, whereas the sulfate source comes from the shallow H_2S oxidation [43].

The acid-sulfate alteration identified, where steam heated overprint on several steam vents, hot springs or mud pools, is the main alteration type in the Furnas craterial area. The acid stage (interaction fluid/trachyte rocks) is characterized by a kaolinite + alunite + halloysite-7Å + opal-A + native sulphur assemblage. The total leaching of cations from primary minerals (i.e., sanidine) of trachyte rocks near the vents, including Al, is due to the pH stabilization in the very acid domain by H_2S oxidation. Under acidic hydrothermal fluids (pH < 4 at 20 °C) circulation in a convective meteoric system, the Al becomes more soluble than silica.
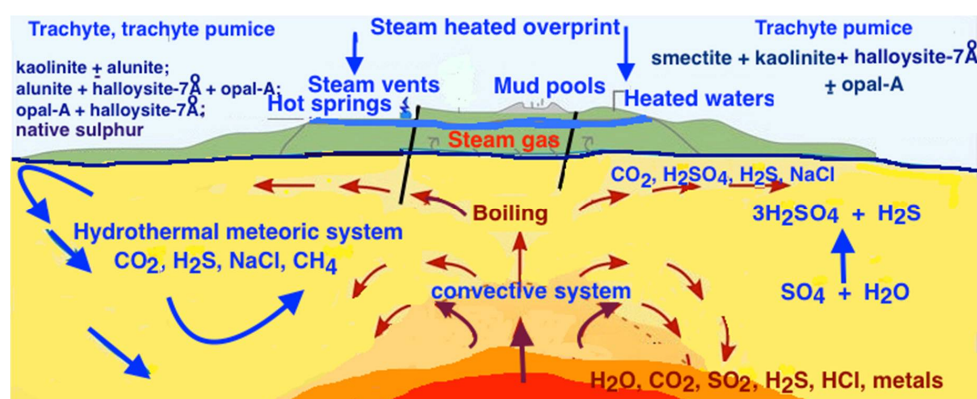

Figure 9. The acid-sulfate alteration adapted model [86] of the active hydrothermal system of Furnas volcano, The Azores Archipelago fluids (pH < 4 at 20 °C) circulation in a convective meteoric system, the Al becomes more soluble than silicon. Low or high supersaturated solution of Si and Al will favor the crystallization of kaolinite or halloysite-7 Å [90].

Since the major part of the Al dissolved in solutions is consumed by alunite precipitation (due to the H_2S oxidation) and the growth of kaolinite is limited [91]. Alunite is the most stable solid phase with respect to solubility controls on Al [92], where the Al concentration in solution is controlled by the growth kinetics of alunite. The Si concentration is independently controlled by the solubility of amorphous silica in particular glassy from pumice rocks. Opal-A lepispheres form in silica-saturated hot-spring fluids, where silica polymerisation promotes growth and precipitation of colloids aggregate to form a friable, porous, weakly cemented deposit occurs in young sinter [93,94].

The presence of smectite in assemblages with alunite + kaolinite from mud pools and steaming grounds (mud clay) near the Furnas lake, suggests different crystallization conditions (intermediate-type system with intermediate ratio Ca^{2+}, Na^+, Mg^{2+}/H^+) than acid sulfate alteration stage previously described. Smectite, beside opal-A, zeolites, etc., is one of the neoformation minerals crystalized during glass alteration [61,62,65] at a low temperature related to a propylitic alteration supposed to occurs below 100 m depth underground. Smectite occurs in a mechanical mixture with kaolinite and alunite crystallized during acid-sulfate stage, probably it being discharged along the fracture zones by hot convective waters.

6. Conclusions

High-field-strain elements and REE provide important insights into the active hydrothermal-meteoric system of Furnas volcano, where their confirmed mobilization within the acid-sulfate alteration was controlled by temperature, pH and solution chemistry. This study shows that HFSE are significantly fractionated in acid low-temperature environment and oxidizing conditions, where higher amounts were stored during acid-sulfate stage formation after the breakdown of pre-existing HFSE-bearing accessory minerals and probably formation of new minerals (i.e., hydrothermal rutile, etc).

Also, the acid-sulfate alteration plays an important role in the REE controlling and fractionation, being a transient REE storage in clays and sulfate minerals. Non-chondritic Y vs. Ho(Dy) displays a clear fractionation generated during fluid migration where different neoformation phases were discriminated within the acid-sulfate stage.

There is no differences of the REE trends between fresh rocks and acid-sulfate rocks where subparallel trends have resulted own to the low alteration intensity and low fluid/rock ratios. Significant negative Eu anomaly (the gull body) observed in all samples (including sinter) confirms a less alteration of Eu-rich feldspar. The REE are differentially mobilized during acid-sulfate alteration where large negative Eu-anomaly and LREE enriched were observed in clay-sulfate assemblages. Kaolin + alunite and smectite + kaolin + alunite (mud) assemblages retained higher amounts of LREE than opal-A + alunite (sinter), whereas the HREE are strongly depleted in sinter.

References

1. Giggenbach, W.F. Magma degassing and mineral deposition in hydrothermal systems along convergent plate boundaries. *Econ. Geol.* **1992**, *97*, 1927–1944.
2. Christenson, B.W.; Wood, C.P. Evolution of a vent-hosted hydrothermal system beneath Ruapehu crater lake, New Zeeland. *Bull. Volcanol.* **1993**, *55*, 547–565. [CrossRef]
3. Delmelle, P.; Bernard, A. Geochemistry, mineralogy, and chemical modelling of the acid crater lake of Kawah Ijen volcano, Indonesia. *Geochim. Cosmochim. Acta* **1994**, *58*, 2445–2460. [CrossRef]
4. Africano, F.; Bernard, A. Acid alteration in the fumarolic environment of Usu volcano, Hokkaido, Japan. *J. Volcanol. Geotherm. Res.* **2000**, *97*, 475–495. [CrossRef]
5. Berger, B.R.; Henley, R.W.; Lowers, H.A.; Pribil, M.J. The Lepanto Cu–Au deposit, Philippines: A fossil hyperacidic volcanic lake complex. *J. Volcanol. Geotherm. Res.* **2014**, *271*, 70–82. [CrossRef]
6. Henley, R.W. Hyperacidic Volcanic Lakes, Metal Sinks and Magmatic Gas Expansion in Arc Volcanoes. In *Volcanic Lakes, Advances in Volcanology*; Springer: Berlin/Heidelberg, Germany, 2015; pp. 155–184. [CrossRef]
7. Giggenbach, W.F. Isotopic shifts in waters from geothermal and volcanic systems along convergent plate boundaries and their origin. *Earth Planet. Sci. Lett.* **1992**, *113*, 495–510. [CrossRef]
8. Hedenquist, J.W.; Aoki, M.; Shinohara, H. Flux of volatiles and ore-forming metals from the magmatic-hydrothermal system of Satsuma Iwojima volcano. *Geology* **1994**, *22*, 585–588. [CrossRef]
9. Symonds, R.B.; Rose, W.I.; Bluth, G.J.S.; Gerlach, T.M. Volcanic-gas studies: Methods, results and applications. *Rev. Mineral.* **1994**, *30*, 1–66.
10. Shinohara, H. A missing link between volcanic degassing and experimental studies on chloride partitioning. *Chem. Geol.* **2009**, *263*, 51–59. [CrossRef]
11. Delmelle, P.; Henley Richard, W.R.; Opfergelt, S.; Detienne, M. Summit Acid Crater Lakes and Flank Instability in Composite Volcanoes. In *Volcanic Lakes*; Springer: Berlin/Heidelberg, Germany, 2015; pp. 289–305. [CrossRef]
12. Muffler, L.J.P. Geothermal reservoir assessment. In *Geothermal Systems: Principles and Case Histories*; Rybach, L., Muffler, L.J.P., Eds.; John Wiley & Sons: Hoboken, NJ, USA, 1981; p. 181.
13. Henley, R.W.; McNabb, A. Magmatic vapor plumes and ground water interaction in porphyry copper emplacement. *Econ. Geol.* **1978**, *73*, 1–20. [CrossRef]
14. Hedenquist, J.W.; Arribas, A.; Reynolds, T.J. Evolution of an intrusion-centered hydrothermal system; Far Southeast-Lepanto porphyry and epithermal Cu-Au deposits, Philippines. *Econ. Geol.* **1998**, *93*, 373–404. [CrossRef]
15. Heald, P.; Foley, N.K.; Hayba, D.O. Comparative anatomy of volcanic hosted epithermal deposits: Acid sulfate and adularia-sericite types. *Econ. Geol.* **1987**, *82*, 1–26. [CrossRef]
16. Hemley, J.J.; Jones, J. Chemical aspects of hydrothermal alteration with emphasis on hydrogen metasomatism. *Econ. Geol.* **1964**, *59*, 538–569. [CrossRef]
17. Hedenquist, J.W.; Lowenstern, J.B. The role of magmas in the formation of hydrothermal ore deposits. *Nature* **1994**, *370*, 519–527. [CrossRef]
18. Herdianita, N.R.; Rodgers, K.A.; Browne, P.R.L. Routine procedures for characterizing modern and ancient silica sinter deposits. *Geothermics* **2000**, *29*, 367–375. [CrossRef]
19. Herdianita, N.R.; Browne, P.R.L.; Rodgers, K.A.; Campbell, A. Mineralogical and textural changes accompanying ageing of silica sinter. *Mineral. Depos.* **2000**, *35*, 48–62. [CrossRef]
20. Hedenquist, J.W.; Taran, Y.A. Modeling the formation of advanced argillic lithocaps: Volcanic vapor condensation above porphyry intrusions. *Econ. Geol.* **2013**, *108*, 1523–1540. [CrossRef]
21. Giggenbach, W.F.; Gonfiantini, R.; Jangi, B.L.; Truesdell, A.H. Isotopic and chemical composition of Parbati Valley geothermal discharges, northwest Himalaya, India. *Geothermics* **1983**, *12*, 199–222. [CrossRef]
22. Inskeep, W.; Nordstrom, D.K.; Mogk, D.; Rodman, A.; Macur, E.E.; Fouke, B.; Durães, N.; Guzman, M. Secondary Minerals associated with thermal soils and geothermal features of Yellowstone National Park. In *Clays of Yellostone Park*; Schroeder, P., Ed.; Clay Minerals Society: Boulder, CO, USA, 2010; pp. 29–47.
23. Piochi, M.; Kilburn, C.R.J.; Di Vito, M.A.; Mormone, A.; Tramelli, A.; Troise, C.; De Natale, G. The volcanic and geothermally active Campi Flegrei caldera: An integrated multidisciplinary image of its buried structure. *Int. J. Earth Sci.* **2014**, *10*, 401–421. [CrossRef]
24. Piochi, M.; Mormone, A.; Balassone, G.; Strauss, H.; Troise, C.; De Natale, G. Native sulfur, sulfates and sulfides from the active Campi Flegrei volcano (southern Italy): Genetic environments and degassing dynamics revealed by mineralogy and isotope geochemistry. *J. Volcanol. Geotherm. Res.* **2015**, *304*, 180–193. [CrossRef]
25. Piochi, M.; Mormone, A.; Balassone, G. Hydrothermal alteration environments in the recent dynamics of the Ischia volcanic island (Southern Italy): Clues from repeated field, mineralogical and geochemical surveys across the 2017 earthquake of Casamicciola. *J. Volcanol. Geotherm. Res.* **2019**, *376*, 104–124. [CrossRef]
26. Shakeri, A.; Ghoreyshinia, S.; Mehrabi, B.; Delavari, M. Rare earth elements geochemistry in springs from Taftan geothermal area SE Iran. *J. Volcanol. Geotherm. Res.* **2015**, *304*, 49–61. [CrossRef]
27. White, D.E.; Hutchinson, R.A.; Keith, T.E.C. *The Geology and Remarkable Thermal Activity of Norris Geyser Basin, Yellowstone National Park, Wyoming*; U.S. Geological Survey (USGS): Reston, VA, USA, 1988; p. 1456.

28. Moore, R. Volcanic geology and eruption frequency, S. Miguel, Azores. *Bull. Volcanol.* **1990**, *52*, 602–614. [CrossRef]
29. Ferreira, T.; Oskarsson, N. Chemistry and isotopic composition of fumarole discharge of Furnas caldera. *J. Volcanol. Geotherm. Res.* **1999**, *92*, 169–179. [CrossRef]
30. Cruz, J.V.; Coutinho, R.M.; Carvalho, M.R.; Oskarsson, N.; Gislason, S.R. Chemistry of waters from Furnas volcano, São Miguel, Azores: Fluxes of volcanic carbon dioxide and leached material. *J. Volcanol. Geotherm. Res.* **1999**, *92*, 151–167. [CrossRef]
31. Searle, R. Tectonic pattern of the Azores spreading centre and triple junction. *Earth Planet Sci. Lett.* **1980**, *51*, 415–434. [CrossRef]
32. Luis, J.F.; Miranda, J.M.; Galdeano, A.; Patriat, P.; Rossignol, J.C.; Mendes Victor, L.A. The Azores triple junction evolution since 10 Ma from an aerogmagnetic survey of mid-Atlantic Ridge. *Earth Planet. Sci. Lett.* **1994**, *125*, 439–459. [CrossRef]
33. Marques, F.O.; Catalão, J.C.; DeMets, C.; Costa, A.C.G.; Hildenbrand, A. GPS and tectonic evidence for a diffuse plate boundary at the Azores Triple Junction. *Earth Planet. Sci. Lett.* **2013**, *381*, 177–187. [CrossRef]
34. Moore, B.R. Geology of three late Quaternary stratovolcanoes on São Miguel, Azores. *U.S. Geol. Surv. Bull.* **1991**, *1900*, 1–46.
35. Walker, G.P.L.; Croasdale, R. Two plinian-type eruptions in the Azores. *J. Geol. Soc. Lond.* **1971**, *127*, 17–55. [CrossRef]
36. Calvert, A.T.C.; Moore, R.B.; McGeehin, J.P.; Rodrigues da Silva, A.M. Volcanic history and ^{40}Ar/^{39}Ar and ^{14}C geochronology of Terceira Island, Azores, Portugal. *J. Volcanol. Geotherm. Res.* **2006**, *156*, 103–115. [CrossRef]
37. Jeffery, A.J.; Gertisser, R.; O'Driscoll, B.; Pacheco, J.M.; Whitley, S.; Pimentel, S.A. Temporal evolution of a post-caldera, mildly peralkaline magmatic system: Furnas volcano, São Miguel, Azores. *Contrib. Mineral. Petrol.* **2016**, *171*, 42–59. [CrossRef]
38. Cole, P.D.; Queiroz, G.; Wallenstein, N.; Gaspar, J.L.; Duncan, A.M.; Guest, J.E. An historic subplinian to phreatomagmatic eruption: The 1630 eruption of Furnas volcano, São Miguel, Azores. *J. Volcanol. Geotherm. Res.* **1999**, *69*, 117–135. [CrossRef]
39. Guest, J.E.; Gaspar, J.L.; Cole, P.D.; Queiroz, G.; Duncan, M.; Wallenstein, N.; Ferreira, T.; Pacheco, J.M. Volcanic geology of Furnas volcano, São Miguel, Azores. *J. Volcanol. Geotherm. Res.* **1999**, *92*, 1–29. [CrossRef]
40. Booth, B.; Walker, G.P.L.; Croasdale, R. A quantitative study of five thousand years of volcanism on São Miguel, Azores. *Philos. Trans. R. Soc. Lond.* **1978**, *228*, 271–319.
41. Guest, J.E.; Pacheco, J.M.; Cole, P.D.; Duncan, A.M.; Wallenstein, N.; Queiroz, G.; Gaspar, J.L.; Ferreira, T. Volcanic geology of São Miguel Island (Azores Archipelago): Introduction. *Geol. Soc. London Mem.* **2015**, *44*, 125–134. [CrossRef]
42. Cruz, J.V.; França, Z. Hydrogeochemistry of thermal and mineral water springs of the Azores archipelago (Portugal). *J. Volcanol. Geotherm. Res.* **2006**, *151*, 382–398. [CrossRef]
43. Zbyszewski, G.; Almeida, F.M.; Ferreira, O.V.; Assunção, C.T. Carta Geológica de Portugal na escala 1:50,000. Notícia explicativa da folha B, S. Miguel (Açores). *Serv. Geol. Port. Lisboa* **1958**, 37.
44. Woitischek, J.; Dietzel, M.; Inguaggiato, C.; Böttcher, M.E.; Leis, L.; Cruz, V.J.; Gehre, M. Characterisation and origin of hydrothermal waters at São Miguel (Azores) inferred by chemical and isotopic composition. *J. Volcanol. Geotherm. Res.* **2017**, *346*, 104–117. [CrossRef]
45. Jones, J.B.; Segnit, E.R. The nature of opal I. Nomenclature and constituent phases. *J. Geol. Soc. Aust.* **1971**, *18*, 57–68. [CrossRef]
46. Flörke, O.W.; Graetsch, H.; Martin, B.; Roller, K.; Wirth, R. Nomenclature of micro- and non-crystalline silica minerals, based on structure and microstructure. *Neues Jahrb. Mineral. Abh.* **1991**, *163*, 19–42.
47. Graetsch, H. Structural characteristics of opaline and microcrystalline silica minerals. In *Silica: Physical Behaviour, Geochemistry and Materials Applications*; Heaney, P.J., Prewitt, C.T., Gibbs, G.V., Eds.; Mineralogical Society of America: Chantilly, VA, USA, 1994; pp. 209–232.
48. Taylor, S.R.; McLennan, S.M. The geochemical evolution of the continental crust. *Rev. Geophisique* **1995**, *33*, 241–265. [CrossRef]
49. Hinckley, D.N. Variability in "crystallinity" values among the kaolin deposits of the coastal plain of Georgia and South Carolina. *Clays Clay Miner.* **1963**, *11*, 229–235. [CrossRef]
50. Bigham, J.M.; Schwertmann, U.; Traina, S.J.; Winland, R.L.; Wolf, M. Schwertmannite and the chemical modeling of iron in acid sulfate waters. *Geochim. Cosmochim. Acta* **1996**, *60*, 185–195. [CrossRef]
51. Marschall, H.R.; Dohmen, R.; Ludwig, T. Diffusion-induced fractionation of niobium and tantalum during continental crust formation. *Earth Planet. Sci. Lett.* **2013**, *375*, 361–371. [CrossRef]
52. Jiang, S.-Y.; Wang, R.-C.; Xu, X.-S.; Zhao, K.-D. Mobility of high field strength elements (HFSE) in magmatic-, metamorphic-, and submarine-hydrothermal systems. *Phys. Chem. Earth* **2005**, *30*, 1020–1029. [CrossRef]
53. Münker, C.; Pfänder, J.A.; Weyer, S.; Buchl, A.; Kleine, T.; Mezger, K. Evolution of planetary cores and the Earth–Moon system from Nb/Ta systematics. *Science* **2003**, *301*, 84–87. [CrossRef]
54. Wood, S.A. The geochemistry of rare earth elements and yttrium in geothermal waters. *Soc. Econ. Geol. Spec. Pub.* **2003**, *10*, 133–158.
55. Peiffer, L.; Taran, Y.; Lounejeva, E.; Solís-Pichardo, E.; Rouwet, D.; Bernard-Romero, R.A. Tracing thermal aquifers of El Chichónn volcano-hydrothermal system (Mexico) with ^{87}Sr/^{87}Sr, Ca/Sr and REE. *J. Volcanol. Geotherm. Res.* **2011**, *205*, 55–66. [CrossRef]
56. Wood, S.A. Rare element systematics of acidic geothermal waters from the Taupo Volcanic Zone, New Zealand. *J. Geochem. Explor.* **2006**, *89*, 424–427. [CrossRef]
57. Fulignati, A.; Gioncada, A.; Sbrana, A. Rare-earth element (REE) behavior in the alteration facies of the active magmatic hydrothermal system of Vulcano (Aeolian Islands, Italy). *J. Volcanol. Geotherm. Res.* **1999**, *88*, 325–342. [CrossRef]
58. Kulaksız, S.; Bau, M. Contrasting behaviour of anthropogenic gadolinium and natural rare earth elements in estuaries and the gadolinium input into the North Sea. *Earth Planet. Sci. Lett.* **2007**, *260*, 361–371. [CrossRef]

59. Bau, M. Controls on the Fractionation of Isovalent Trace Elements in Magmatic and Aqueous Systems: Evidence from Y/Ho, Zr/Hf and lanthanide tetrad effect. *Contrib. Mineral. Petrol.* **1996**, *123*, 323–333. [CrossRef]

60. Bobos, I.; Gomes, C. Greisen and post-greisen alteration in the São Vicente de Pereira area. *Can. Mineral.* **1998**, *36*, 1615–1624.

61. Bobos, I.; Duplay, J.; Rocha, J.; Gomes, C. Kaolinite to halloysite-7Å transformation in the kaolin deposit of São Vicente de Pereira, Portugal. *Clays Clay Miner.* **2001**, *49*, 597–605. [CrossRef]

62. Gomes, C.S.F.; Massa, M.E. Allophane and sperullitic halloysite, weathering products of trachitic pumice fall-outs in the Caldeira Velha /S.Miguel-Azores). *Miner. Petrog. Acta* **1992**, *XXXVA*, 283–288.

63. Hay, R.L.; Iijima, A. Nature and origin of palagonite tuffs of the Honolulu group on Oahu, Hawaii. *Mem. Geol. Soc. Am.* **1968**, *116*, 331–376.

64. Tomita, K.; Yamane, H.; Kawano, M. Synthesis of Smectite from volcanic glass at low temperature. *Clays Clay Miner.* **1993**, *41*, 655–661. [CrossRef]

65. Berger, G.; Meunier, A.; Beaufort, D. Clay mineral formation on Mars: Chemical constraints and possiblecontribution of basalt out-gassing. *Planet. Space Sci.* **2014**, *95*, 25–32. [CrossRef]

66. Berger, G.; Toplis, M.J.; Treguier, E.; d'Uston, C.; Pinet, P. Evidence in favor of small amounts of ephemeral and transient water during alteration at Meridiani Planum, Mars. *Am. Mineral.* **2009**, *94*, 1279–1282. [CrossRef]

67. Mormone, A.; Ghiara, M.R.; Balassone, G.; Poichi, M.; Lonis, R.; Rossi, M. High-silica zeolites in pyroclastic flows from Central Sardinia (Italy): Clues on genetic processes and reserves from a mineralogical study. *Miner. Petrol.* **2018**, *112*, 767–788. [CrossRef]

68. Ikehata, I.; Maruoka, T. Sulfur isotopic characteristics of volcanic products from the September 2014 Mount Ontake eruption, Japan. *Earth Planets Space* **2016**, *68*, 116. [CrossRef]

69. Williams, S.N.; Sturchio, N.C.; Calvache, V.M.L.; Mendez, R.F.; Londoñ, C.A.; Garcia, N.P. Sulfur dioxide from Nevado del Ruiz volcano, Columbia: Total flux and isotopic constraints on its origin. *J. Volcanol. Geotherm. Res.* **1990**, *42*, 53–68. [CrossRef]

70. Raymahashay, B.C. A geochemical study of rock alteration by hot springs in the Paint Pot Hill area, Yellowstone Park. *Geochim. Cosmochim. Acta* **1968**, *32*, 499–522. [CrossRef]

71. Barker, W.W.; Welch, S.A.; Chu, S.; Banfield, J.F. Experimental observations of the effects of bacteria on aluminosilicate weathering. *Am. Mineral.* **1998**, *83*, 1551–1563. [CrossRef]

72. Monterroso, C.; Alvarez, E.; Macías, F. Speciation and solubility control of Al and Fe in mine soil solutions. *Sci. Total Environ.* **1994**, *158*, 31–43. [CrossRef]

73. Durães, N.; Bobos, I.; Ferreira da Silva, E. Speciation and precipitation of heavy metals in the acid mine waters from the Iberian Pyrite Belt (Portuguese sector). *Environ. Sci. Pollut. Res.* **2017**, *24*. [CrossRef] [PubMed]

74. Nordstrom, D.K. Aqueous pyrite oxidation and the consequent formation of secondary iron minerals. *Acid Sulfate Weather* **1982**, *10*, 37–56.

75. Finlow-Bates, T.; Stumpfl, E.F. The behaviour of so-called immobile elements in hydrothermally altered rocks associated with volcanogenic submarine-exhalative ore deposits. *Miner. Deposita.* **1981**, *16*, 319–328. [CrossRef]

76. Rubin, J.N.; Henry, C.D.; Price, J.G. The mobilization of zirconium and other "immobile" elements during hydrothermal alteration. *Chem. Geol.* **1993**, *110*, 29–47. [CrossRef]

77. Aja, S.U.; Wood, S.A.; Williams-Jones, A.E. The aqueous geochemistry of Zr and the solubility of some Zr-bearing minerals. *Appl. Geochem.* **1995**, *10*, 603–620. [CrossRef]

78. Brown, P.; Curti, E.; Grambow, B. *Chemical Thermodynamics of Zirconium*; Elsevier: Amsterdam, The Netherlands, 2005. Available online: http://www.oecdnea.org/dbtdb/pubs/vol8-zirconium.pdf (accessed on 23 March 2021).

79. Michard, A. Rare earth element systematics in hydrothermal fluids. *Geochim. Cosmochim. Acta* **1989**, *53*, 745–750. [CrossRef]

80. Lottermoser, B.G. Rare earth elements and hydrothermal ore formation processes. *Ore Geol. Rev.* **1992**, *7*, 25–41. [CrossRef]

81. Alderton, D.H.M.; Pearce, J.A.; Potts, P.J. Rare earth element mobility during granite alteration: Evidence from southeast England. *Earth Planet. Sci. Lett.* **1980**, *49*, 149–165. [CrossRef]

82. Inguaggiato, C.; Censi, P.; Zuddas, P.; Londoño, J.M.; Chacón, Z.; Alzate, D.; Brusca, L.; D'Alessandro, W. Zirconium–hafnium and rare earth element signatures discriminating the effect of atmospheric fallout from hydrothermal input in volcanic lake water. *Chem. Geol.* **2016**, *433*, 1–11. [CrossRef]

83. Sverjensky, D.A. Europium redox equilibria in aqueous solution. *Earth Planet. Sci. Lett.* **1984**, *67*, 70–78. [CrossRef]

84. Bau, M. Rare-earth element mobility during hydrothermal and metamorphic fluid–rock interaction and the significance of the oxidation state of europium. *Chem. Geol.* **1991**, *93*, 219–230. [CrossRef]

85. Lewis, A.J.; Palmer, M.A.; Sturchio, N.C.; Kemp, A.J. The rare earth element geochemistry of acid-sulfate and acid-sulfate-chloride geothermal systems from Yellowstone National Park, Wyoming, USA. *Geochim. Cosmochim. Acta* **1997**, *61*, 695–706. [CrossRef]

86. Leybourne, M.I.; Goodfellow, W.D.; Boyle, D.R. Hydrogeochemical, isotopic and rare earth element geochemistry of acid–sulphate and acid–sulphate–chloride geothermal systems from Yellowstone. *Geochim. Cosmochim. Acta* **2000**, *61*, 695–723. [CrossRef]

87. Wan, Y.; Liu, C. The effect of humic acid on the adsorption of REE on kaolin. *Colloids Surf. A Physicochem. Eng. Asp.* **2006**, *290*, 112–117. [CrossRef]

88. Coppin, F.; Berger, G.; Bauer, A.; Castet, S.; Loubet, M. Sorption of lanthanides on smectite and kaolinite. *Chem. Geol.* **2002**, *182*, 57–68. [CrossRef]

89. Ellis, A.J.; Mahon, W.A. *Geochemistry of Geothermal Systems*; Academic Press: New York, NY, USA, 1977; p. 392. [CrossRef]

90. Merino, E.; Harvey, C.; Murray, H.H. Aqueous-Chemical Control of the Tetrahedral-Aluminum Content of Quartz, Halloysite, and other Low-Temperature Silicates. *Clays Clay Miner.* **1989**, *37*, 135–142. [CrossRef]
91. Inoue, A.; Aoki, M.; Ito, H. Mineralogy of Ohyunuma explosion crater lake, Kokkaido, Japan. *Clay Sci.* **2000**, *11*, 169–187.
92. Sposito, G. *Chemical Equilibria and Kinetics in Soils*; Oxford University Press: Oxford, UK, 1994; p. 260.
93. Rimstidt, J.D.; Cole, D.R. Geothermal mineralization I: The mechanism of formation of the Beowawe, Nevada, siliceous sinter deposit. *Am. J. Sci.* **1983**, *283*, 861–875. [CrossRef]
94. Fournier, R.O. The behaviour of silica in hydrothermal solutions. In *Geology and Geochemistry of Epithermal Systems*; Society of Economic Geologists: Littleton, CO, USA, 1985; pp. 45–60.